A Broadband Potential-Based Boundary Element Method for Modeling Electromagnetic Scattering from Dielectrics and Conductors

Shashwat Sharma, Piero Triverio
Edward S. Rogers Sr. Department of Electrical and Computer Engineering, University of Toronto, Canada
shash.sharma@mail.utoronto.ca, piero.triverio@utoronto.ca

***Abstract*—We present a boundary element method for electromagnetic scattering analysis, formulated in terms of the magnetic vector and electric scalar potentials rather than electromagnetic fields. The proposed potential-based formulation does not rely on the mutual coupling between electric and magnetic fields, and is therefore able to simulate dielectric objects over a wider range of frequency than is possible with state-of-the-art field-based methods, as demonstrated via numerical examples.**

***Index Terms*—surface integral equations, electromagnetic potentials, electromagnetic scattering, dielectrics.**

I. Introduction

Electromagnetic solvers are essential for modeling dielectric objects in applications ranging from antenna design [1] to the analysis of metasurfaces with dielectric unit cells [2], [3]. The boundary element method (BEM) [4] is a promising technique for the electromagnetic analysis of dielectric objects because it avoids the need for a 3D mesh throughout the simulation domain, as in the finite element method [5]; instead, the BEM requires only a 2D mesh for the surface of each object.

Most full-wave BEM formulations involve electric and magnetic fields as unknown quantities, and rely on their mutual coupling. Consequently, the decoupling of electric and magnetic fields in the static limit can cause either numerical instability [6] or inaccuracy [7] at very low frequencies. Recently, BEM formulations for scattering analysis were developed in terms of electromagnetic potentials rather than fields [8]–[10], which remain valid even in the static limit. However, most potential-based integral equation (PIE) formulations are applicable only to perfect electric conductors [8], [11], [12]. A PIE formulation for dielectric objects was studied from a theoretical perspective in [10], but a discussion about the discretization of the problem was not provided. Furthermore, the formulation in [10] is similar to the classical PMCHWT [13]–[15] approach, in that integral equations associated with adjacent materials are linearly combined, which may lead to inaccuracy in the case of a large contrast in material properties.

A new PIE formulation was proposed in [16] for modeling electromagnetic scattering from objects of arbitrary conductivity. Here, we demonstrate that this formulation is also applicable to lossless dielectrics over an extremely wide range of frequencies, beyond the capabilities of state-of-the-art BEM formulations based on fields. Although some field-based formulations can model conductive objects across a wide frequency band [16], [17], they can become inaccurate for dielectrics at very low frequencies unless specialized techniques are used [7]. This may limit the ability of field-based methods to model devices with sub-wavelength dielectric elements [2], [3]. In contrast, the proposed potential-based formulation is accurate for both lossless and lossy objects of arbitrary conductivity, across an extremely wide range of frequency, without any special treatment in the near-static regime. In the proposed method, both the scalar and vector potential integral equations [9] are coupled and solved simultaneously in the regions internal and external to each object. Unlike the examples considered in [16], here we identify cases where state-of-the-art field-based methods become inaccurate compared to the potential-based approach. Unlike [16], we also discuss practical considerations such as the evaluation of surface integrals and the recovery of surface tangential fields from the computed potentials, for post-processing purposes.

II. PIE Formulation for Dielectrics

Consider an object with permittivity ε and permeability μ, occupying volume $\mathcal{V}$, with surface $\mathcal{S}$ and outward unit normal vector $\hat{n}$. The object resides in free space, $\mathcal{V}_0$, with permittivity ε_0 and permeability μ_0. The goal is to derive a suitable set of surface integral equations to compute the vector magnetic and electric scalar potentials, $\vec{A}(\vec{r})$ and $\phi(\vec{r})$, respectively.

A. Internal Region

Using the Lorenz gauge [18]

$$\nabla \cdot \vec{A}(\vec{r}) = -j\omega\varepsilon\mu\,\phi(\vec{r}), \tag{1}$$

where ω is the angular frequency, leads to a pair of Helmholtz equations for $\vec{A}(\vec{r})$ and $\phi(\vec{r})$ [8], [9], [18],

$$\nabla^2\vec{A}(\vec{r}) + k^2\vec{A}(\vec{r}) = 0, \tag{2}$$

$$\nabla^2\phi(\vec{r}) + k^2\phi(\vec{r}) = 0, \tag{3}$$

where $k = \omega\sqrt{\varepsilon\mu}$ is the wave number associated with $\mathcal{V}$. Green's identities [19] can then be used to derive the surface integral equations [9]

$$\begin{aligned}\mathcal{L}\big[\hat{n}'\times\nabla'\times\vec{A}(\vec{r}')\big] + \mathcal{K}\big[\hat{n}'\times\vec{A}(\vec{r}')\big] \\ + \vec{A}(\vec{r}) + j\omega\varepsilon\mu\,\mathcal{L}\big[\phi(\vec{r}')\hat{n}'\big] \\ - \nabla\mathcal{L}\big[\hat{n}'\cdot\vec{A}(\vec{r}')\big] = 0,\end{aligned} \tag{4}$$

and

$$\mathcal{L}\big[\hat{n}' \cdot \nabla\phi\left(\vec{r}'\right)\big] + \mathcal{M}\big[\phi\left(\vec{r}'\right)\big] - \phi\left(\vec{r}\right) = 0, \tag{5}$$

where primed and unprimed coordinates denote source and observation points, respectively, $\vec{r} \in \mathcal{V}$, and $\vec{r}' \in \mathcal{S}^-$, with $\mathcal{S}^-$ denoting the inner surface of $\mathcal{S}$. The integral operators used in (4) and (5) are defined in [16]. Term $G\left(k, \vec{r}, \vec{r}'\right)$ is the Green's function associated with the object's material,

$$G\left(k, \vec{r}, \vec{r}'\right) = \frac{e^{-jk\left|\vec{r}-\vec{r}'\right|}}{4\pi\left|\vec{r}-\vec{r}'\right|}. \tag{6}$$

Letting $\vec{r} \to \mathcal{S}^-$, two independent surface integral equations can be derived from (4) by taking its tangential component,

$$\begin{aligned}\hat{n} \times \mathcal{L}\big[\hat{n}' \times \nabla' \times \vec{A}\left(\vec{r}'\right)\big] + \hat{n} \times \cancel{\mathcal{K}}\big[\hat{n}' \times \vec{A}\left(\vec{r}'\right)\big] \\ + \frac{1}{2}\,\hat{n} \times \vec{A}\left(\vec{r}\right) + j\omega\varepsilon\mu\,\hat{n} \times \mathcal{L}\big[\phi\left(\vec{r}'\right)\hat{n}'\big] \\ - \hat{n} \times \nabla\mathcal{L}\big[\hat{n}' \cdot \vec{A}\left(\vec{r}'\right)\big] = 0,\end{aligned} \tag{7}$$

and its normal component,

$$\begin{aligned}\hat{n} \cdot \mathcal{L}\big[\hat{n}' \times \nabla' \times \vec{A}\left(\vec{r}'\right)\big] + \hat{n} \cdot \cancel{\mathcal{K}}\big[\hat{n}' \times \vec{A}\left(\vec{r}'\right)\big] \\ + \frac{1}{2}\,\hat{n} \cdot \vec{A}\left(\vec{r}\right) + j\omega\varepsilon\mu\,\hat{n} \cdot \mathcal{L}\big[\phi\left(\vec{r}'\right)\hat{n}'\big] \\ - \hat{n} \cdot \nabla\mathcal{L}\big[\hat{n}' \cdot \vec{A}\left(\vec{r}'\right)\big] = 0,\end{aligned} \tag{8}$$

where a dash through an operator indicates that the associated integral is computed in the principal value sense [4].

Together, (7), (8) and (5) model the physics inside $\mathcal{V}$. These equations are discretized as follows. A triangular mesh is generated for the surface of the object, and the expansion functions are chosen so that they respect the mutual orthogonality of the unknowns $\hat{n} \times \nabla \times \vec{A}\left(\vec{r}\right)$ and $\hat{n} \times \vec{A}\left(\vec{r}\right)$. To this end, $\hat{n} \times \nabla \times \vec{A}\left(\vec{r}\right)$ is expanded with the Rao-Wilton-Glisson (RWG) functions [20] $\vec{f}_n\left(\vec{r}\right)$, while $\hat{n} \times \vec{A}\left(\vec{r}\right)$ is expanded with the Buffa-Christiansen (BC) functions [21], [22] $\vec{g}_n\left(\vec{r}\right)$, which are defined on a barycentric refinement of the mesh. This choice was inspired by the discretization scheme in [23] and ensures that the mutual orthogonality of $\hat{n} \times \nabla \times \vec{A}\left(\vec{r}\right)$ and $\hat{n} \times \vec{A}\left(\vec{r}\right)$ is respected by the basis functions, leading to well conditioned matrix blocks. The remaining unknowns are scalar, and are expanded with pulse basis functions $h_n\left(\vec{r}\right)$. For $\hat{n}\cdot\nabla\phi\left(\vec{r}\right)$ in (5), the pulse functions are normalized by the area of the associated mesh triangle, which improves the condition number of the final system matrix [16]. Equation (7) is then tested with $\hat{n} \times$ RWG functions, while (8) and (5) are tested with area-normalized pulse basis functions. Thus, the discrete versions of (7), (8) and (5) are obtained,

$$\begin{aligned}\mathbf{L}^{(\mathrm{ff})}\mathbf{a}_{c,} + \left(\cancel{\mathbf{K}}^{(\mathrm{fg})} + \frac{1}{2}\,\mathbf{I}_{\times}^{(\mathrm{fg})}\right)\mathbf{a}_{t,} \\ + j\omega\varepsilon\mu\,\mathbf{L}^{(\mathrm{fh})}\mathbf{\Phi} + \mathbf{D}^T\mathbf{L}^{(\mathrm{hh})}\mathbf{a}_{n,} = \mathbf{0},\end{aligned} \tag{9}$$

$$\begin{aligned}\mathbf{L}^{(\mathrm{hf})}\mathbf{a}_{c,} + \cancel{\mathbf{K}}^{(\mathrm{hg})}\mathbf{a}_{t,} + j\omega\varepsilon\mu\,\mathbf{L}^{(\mathrm{hh})}\mathbf{\Phi} \\ - \left(-\left(\cancel{\mathbf{M}}^{(\mathrm{hh})}\right)^T - \frac{1}{2}\mathbf{I}_{\|}^{(\mathrm{hh})}\right)\mathbf{a}_{n,} = \mathbf{0},\end{aligned} \tag{10}$$

and

$$\mathbf{L}^{(\mathrm{hh})}\mathbf{\Psi} + \left(\cancel{\mathbf{M}}^{(\mathrm{hh})} - \frac{1}{2}\mathbf{I}_{\|}^{(\mathrm{hh})}\right)\mathbf{\Phi} = \mathbf{0}, \tag{11}$$

respectively, where the superscript "T" denotes the matrix transpose. Matrices $\mathbf{L}$, $\cancel{\mathbf{K}}$ and $\cancel{\mathbf{M}}$ are the discretized $\mathcal{L}$, $\cancel{\mathcal{K}}$ and $\cancel{\mathcal{M}}$ operators, respectively, where $\cancel{\mathcal{M}}$ represents $\mathcal{M}$ computed in a principal value sense. The operator $\mathbf{I}_{\times}^{(\mathrm{fg})}$ is the well-conditioned Gram matrix linking $\vec{g}_n\left(\vec{r}\right)$ and $\hat{n} \times \vec{f}_n\left(\vec{r}\right)$, while $\mathbf{I}_{\|}^{(\mathrm{hh})}$ involves testing $h_n\left(\vec{r}\right)$ with $\widetilde{h}_n\left(\vec{r}\right)$, where the tilde denotes normalization by triangle areas. The superscript on each matrix represents the associated pair of testing and basis functions. Column vectors $\mathbf{a}_{c,}$, $\mathbf{a}_{t,}$, $\mathbf{a}_{n,}$, $\mathbf{\Phi}$ and $\mathbf{\Psi}$ contain the unknown coefficients associated with $\hat{n} \times \nabla \times \vec{A}\left(\vec{r}\right)$, $\hat{n} \times \vec{A}\left(\vec{r}\right)$, $\hat{n} \cdot \vec{A}\left(\vec{r}\right)$, $\phi\left(\vec{r}\right)$ and $\hat{n} \cdot \nabla\phi\left(\vec{r}\right)$, respectively.

An important consideration in assembling the matrices in (9)–(11) is the accuracy of numerical integration. Matrices $\mathbf{L}^{(\mathrm{hf})}$ and $\cancel{\mathbf{K}}^{(\mathrm{hg})}$ are particularly sensitive to the integration accuracy, because they involve testing functions which are not in the correct range space for the associated integral operator, and thus rank deficient. Therefore, we employ the specialized polar coordinate integration technique proposed in [24] for all discrete integral operators in (9)–(11), to ensure the accuracy of the final result even for large values of ε.

B. External Region

The procedure in Section II-A can be repeated for the external region. This time, we take the divergence of the surface integral equation rather than its normal component. This choice was found to provide better numerical stability and accuracy at low frequencies [16]. The resulting discrete equations are

$$\begin{aligned}\mathbf{L}_0^{(\mathrm{ff})}\mathbf{a}_{c,0} + \left(\cancel{\mathbf{K}}_0^{(\mathrm{fg})} - \frac{1}{2}\,\mathbf{I}_{\times}^{(\mathrm{fg})}\right)\mathbf{a}_{t,0} \\ + \mu_0\left(j\omega\varepsilon_0\right)\mathbf{L}_0^{(\mathrm{fh})}\mathbf{\Phi}_0 + \mathbf{D}^T\mathbf{L}_0^{(\mathrm{hh})}\mathbf{a}_{n,0} = -\mathbf{a}_{t,\mathrm{inc}},\end{aligned} \tag{12}$$

$$\begin{aligned}\mathbf{L}_0^{(\mathrm{hh})}\mathbf{D}\mathbf{a}_{c,0} + \mu_0\left(j\omega\varepsilon_0\right)\left(\cancel{\mathbf{M}}_0^{(\mathrm{hh})} + \frac{1}{2}\,\mathbf{I}_{\|}^{(\mathrm{hh})}\right)\mathbf{\Phi}_0 \\ + k_0^2\,\mathbf{L}_0^{(\mathrm{hh})}\mathbf{a}_{n,0} = \mu_0\left(j\omega\varepsilon_0\right)\mathbf{\Phi}_{\mathrm{inc}},\end{aligned} \tag{13}$$

$$\mathbf{L}_0^{(\mathrm{hh})}\mathbf{\Psi}_0 + \left(\cancel{\mathbf{M}}_0^{(\mathrm{hh})} + \frac{1}{2}\mathbf{I}_{\|}^{(\mathrm{hh})}\right)\mathbf{\Phi}_0 = -\mathbf{\Phi}_{\mathrm{inc}}, \tag{14}$$

where the subscript "0" indicates quantities associated with the external region $\mathcal{V}_0$. Subscript "inc" indicates quantities associated with incident potentials [8], [9].

C. Final System Matrix

To obtain the final system of equations, an appropriate set of boundary conditions must first be applied. Boundary conditions for the potential-based unknowns were proposed

in [9], [10]. However, for $\hat{n} \cdot \vec{A}(\vec{r})$ and $\hat{n} \cdot \nabla\phi(\vec{r})$, we use a less strict condition compared to [9], [10],

$$-j\omega\left[\varepsilon_0 \hat{n} \cdot \vec{A}_0(\vec{r}) - \varepsilon \hat{n} \cdot \vec{A}(\vec{r})\right] - \left[\varepsilon_0 \hat{n} \cdot \nabla\phi_0(\vec{r}) - \varepsilon \hat{n} \cdot \nabla\phi(\vec{r})\right] = 0, \quad (15)$$

which is derived from the boundary condition for the normal component of the electric flux density, unlike the related condition proposed in [16], which also uses the 2-D continuity equation to account for the conduction current. Equation (15) is used to eliminate $\hat{n} \cdot \nabla\phi(\vec{r})$ from (5). Finally, (12), (9), (13), (10), (11) and (14) are concatenated to get the final system matrix (16) shown at the top of the next page. In (16), ξ is the average mesh edge length, $\gamma_0 = j\omega\varepsilon_0\mu_0$, and $\gamma = j\omega\varepsilon\mu$.

D. Post Processing

Once the system (16) has been solved, the tangential electric field $\hat{n}_0 \times \vec{E}_0(\vec{r})$ and tangential magnetic field $\hat{n}_0 \times \vec{H}_0(\vec{r})$ on the outer side of $\mathcal{S}$ can be recovered in order to compute near- and far-field parameters such as the radar cross section (RCS) and directivity [25]. For this purpose, the following relations can be used:

$$\hat{n}_0 \times \vec{H}_0(\vec{r}) = \frac{1}{\mu_0}\hat{n} \times \nabla \times \vec{A}_0(\vec{r}), \quad (17)$$

$$\hat{n}_0 \times \vec{E}_0(\vec{r}) = -j\omega\,\hat{n} \times \vec{A}_0(\vec{r}) - \hat{n} \times \nabla\phi_0(\vec{r}). \quad (18)$$

We express $\hat{n}_0 \times \vec{H}_0(\vec{r})$ in terms of RWG functions and $\hat{n}_0 \times \vec{E}_0(\vec{r})$ in terms of BC functions, to be consistent with the expansions for $\hat{n} \times \nabla \times \vec{A}_0(\vec{r})$ and $\hat{n} \times \vec{A}(\vec{r})$, respectively. The unknowns associated with $\hat{n}_0 \times \vec{H}_0(\vec{r})$, contained in $\mathbf{H}_0$, are readily computed via the discrete version of (17),

$$\mathbf{H}_0 = \frac{1}{\mu_0}\mathbf{a}_{c,0}. \quad (19)$$

Computing the unknowns associated with $\hat{n}_0 \times \vec{E}_0(\vec{r})$, contained in $\mathbf{E}_0$, requires a careful treatment of the second term on the right-hand side of (18),

$$\mathbf{E}_0 = -j\omega\,\mathbf{a}_{t,} - {\mathbf{I}_{\times}^{(\mathrm{fg})}}^{-1}\mathbf{D}^T\mathbf{I}_{\parallel}^{(\mathrm{hh})}\mathbf{\Phi}, \quad (20)$$

where the inverse of the extremely sparse $\mathbf{I}_{\times}^{(\mathrm{fg})}$ does not need to be computed explicitly; instead, $\mathbf{I}_{\times}^{(\mathrm{fg})}$ is factorized and the second term on the right-hand side of (20) is computed as the solution to a linear system of equations.

III. Results

We consider two numerical examples to demonstrate the accuracy of the proposed formulation for modeling dielectric objects. In particular, we demonstrate that this method can provide accurate results over a broader band of frequencies compared to state-of-the-art field-based BEM formulations such as the generalized impedance boundary condition (GIBC) [24] and the enhanced augmented electric field integral equation (eAEFIE) [23] for dielectrics. Due to the relatively large number of unknown quantities in (16) compared to field-based techniques [23], [24], the computational cost of solving (16) is expected to be higher than that associated with the GIBC [24] and the eAEFIE [23]. However, this added expense may be worth the increased stability and accuracy at low frequencies, and can be alleviated with the use of acceleration algorithms coupled with an iterative solver [26]–[28]. The goal of this work is to study the accuracy of the proposed method compared to existing techniques, so a direct solver based on LU factorization is used to solve (16). A performance comparison using acceleration algorithms to handle large problems will be the subject of future work.

A. Sphere

We consider a dielectric sphere with a diameter of 1 m and a relative permittivity of 4, meshed with $1,346$ triangles and excited by an incident plane wave. The bistatic RCS in the $\vec{E}$-plane is compared against the one obtained with analytical Mie series, the GIBC [24], and the eAEFIE [23], as shown in Fig. 1. We considered a broad range of frequencies from 1 Hz to 300 MHz. Fig. 1 demonstrates the excellent accuracy of the proposed formulation compared with the analytical Mie series in all cases. Furthermore, both the GIBC and eAEFIE formulations become inaccurate at low frequencies. It has been reported in the literature that a perturbation technique [7] can be used to improve the accuracy of the eAEFIE formulation at very low frequencies [23]; evidently, the proposed method does not require such a treatment.

B. Split Ring Resonator Array

Next, we consider the 2×2 array of split ring resonators (SRRs) shown in Fig. 2, which are relevant in metamaterial and metasurface applications [2], [29]. Each element has relative permittivity 11, and the dimensions are identical to the structure studied in [16]. A mesh with $3,392$ triangles is generated, and the structure is excited at 1 THz with an incident plane wave with the electric field polarized in the y direction. Fig. 3 shows the electric field magnitude as measured along the line probe visualized in Fig. 2. The probe is placed along the x axis in the xz plane bisecting the array, $0.4\,\mu\mathrm{m}$ above it. Good agreement is observed between the proposed method and the eAEFIE formulation, while the GIBC is unable to provide accurate results.

Finally, we include an analysis of the SRR array for different values of conductivity σ to demonstrate the versatility of the potential-based approach described here and in [16]. Fig. 4 shows the electric field along the probe line for conductivities of 1 S/m, 10^3 S/m, and 10^6 S/m. Good agreement with the eAEFIE is observed in all cases.

IV. Conclusion

In this work, we described a boundary element method formulated in terms of the magnetic vector and electric scalar potentials. Unlike existing potential-based methods, which were primarily developed for conductors, the proposed formulation is applicable to objects with arbitrary conductivity and geometry over an extremely wide range of frequency. In

$$\begin{bmatrix} \frac{1}{\xi}\mathbf{L}_0^{(\mathrm{ff})} & \mathbf{K}_0^{(\mathrm{fg})} - \frac{1}{2}\mathbf{I}_\times^{(\mathrm{fg})} & \frac{jk_0}{\xi}\mathbf{L}_0^{(\mathrm{fh})} & \mathbf{0} & \frac{1}{\xi}\mathbf{D}^T\mathbf{L}_0^{(\mathrm{hh})} & \mathbf{0} \\ \frac{\mu}{\xi\mu_0}\mathbf{L}^{(\mathrm{ff})} & \mathbf{K}^{(\mathrm{fg})} + \frac{1}{2}\mathbf{I}_\times^{(\mathrm{fg})} & \frac{c_0\gamma}{\xi}\mathbf{L}^{(\mathrm{fh})} & \frac{1}{\xi}\mathbf{D}^T\mathbf{L}^{(\mathrm{hh})} & \mathbf{0} & \mathbf{0} \\ \mathbf{L}_0^{(\mathrm{hh})}\mathbf{D} & \mathbf{0} & jk_0\left(\mathbf{M}_0^{(\mathrm{hh})} + \frac{1}{2}\mathbf{I}_\parallel^{(\mathrm{hh})}\right) & \mathbf{0} & k_0^2\mathbf{L}_0^{(\mathrm{hh})} & \mathbf{0} \\ \frac{\mu}{\mu_0}\mathbf{L}^{(\mathrm{hf})} & \xi\mathbf{K}^{(\mathrm{hg})} & c_0\gamma\mathbf{L}^{(\mathrm{hh})} & \left(\mathbf{M}^{(\mathrm{hh})}\right)^T - \frac{1}{2}\mathbf{I}_\parallel^{(\mathrm{hh})} & \mathbf{0} & \mathbf{0} \\ \mathbf{0} & \mathbf{0} & \mathbf{M}^{(\mathrm{hh})} - \frac{1}{2}\mathbf{I}_\parallel^{(\mathrm{hh})} & \frac{k^2}{\gamma c_0}\mathbf{L}^{(\mathrm{hh})} & -\frac{k_0^2}{\gamma c_0}\frac{\mu}{\mu_0}\mathbf{L}^{(\mathrm{hh})} & \frac{\gamma_0}{\gamma c_0}\frac{\mu}{\mu_0}\mathbf{L}^{(\mathrm{hh})} \\ \mathbf{0} & \mathbf{0} & -\left(\mathbf{M}_0^{(\mathrm{hh})}\right)^T + \frac{1}{2}\mathbf{I}_\parallel^{(\mathrm{hh})} & \mathbf{0} & \mathbf{0} & \frac{1}{c_0}\mathbf{L}_0^{(\mathrm{hh})} \end{bmatrix} \begin{bmatrix} \mathbf{a}_{c,0} \\ \frac{\mathbf{a}_{t,}}{\xi} \\ \frac{\mathbf{\Phi}}{c_0} \\ \mathbf{a}_{n,} \\ \mathbf{a}_{n,0} \\ \mathbf{\Psi}_0 \end{bmatrix} = \begin{bmatrix} \frac{-\mathbf{a}_{t,\mathrm{inc}}}{\xi} \\ \mathbf{0} \\ \gamma_0\mathbf{\Phi}_{\mathrm{inc}} \\ \mathbf{0} \\ \mathbf{0} \\ \frac{-\mathbf{\Phi}_{\mathrm{inc}}}{c_0} \end{bmatrix}. \tag{16}$$

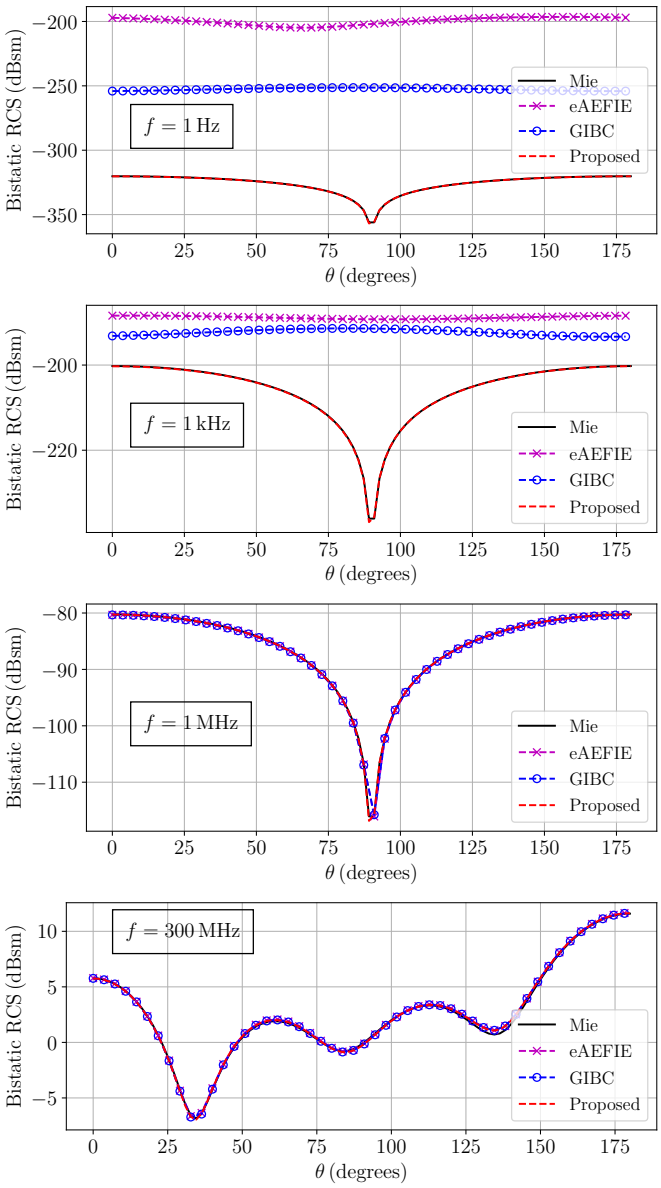

Fig. 1. Accuracy validation for the sphere in Section III-A.

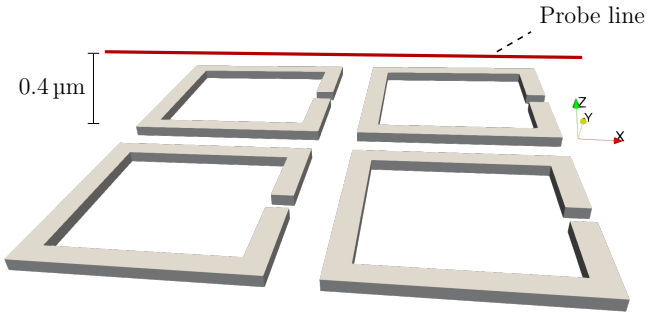

Fig. 2. Geometry of the SRR array in Section III-B.

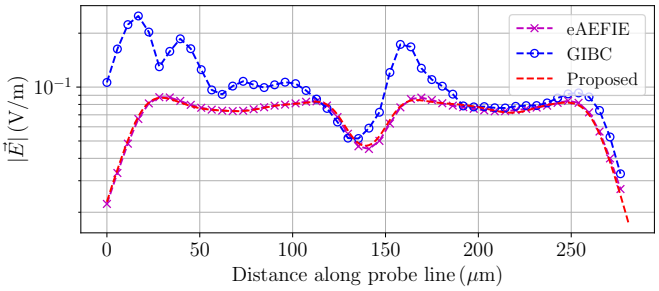

Fig. 3. Near-field $|\vec{E}(\vec{r})|$ for the SRR array in Section III-B.

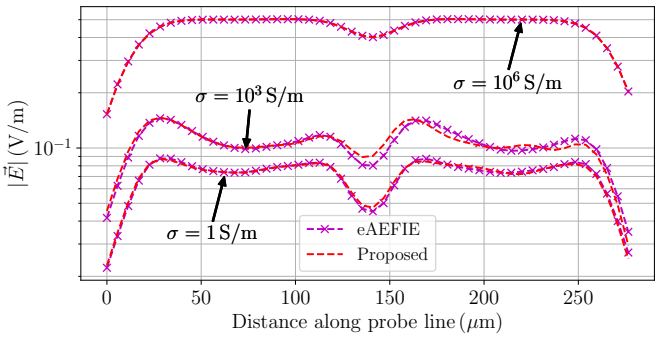

Fig. 4. Near-field $|\vec{E}(\vec{r})|$ for the SRR array in Section III-B for different values of conductivity.

particular, we show that this method remains accurate at very low frequencies even for lossless dielectrics, unlike state-of-the-art formulations based on fields. Practical aspects such as the recovery of electric and magnetic fields for post-processing were discussed. Numerical examples demonstrated the extremely wideband capabilities of the proposed formulation compared to existing field-based formulations.

REFERENCES

[1] A. Petosa, A. Ittipiboon, Y. M. M. Antar, D. Roscoe, and M. Cuhaci, "Recent advances in dielectric-resonator antenna technology," *IEEE Antennas Propag. Mag.*, vol. 40, no. 3, pp. 35–48, Jun. 1998.

[2] A. Tittl, A. Leitis, M. Liu, F. Yesilkoy, D.-Y. Choi, D. N. Neshev, Y. S. Kivshar, and H. Altug, "Imaging-based molecular barcoding with pixelated dielectric metasurfaces," *Science*, vol. 360, no. 6393, pp. 1105–1109, 2018.

[3] C. Zou, G. Ren, M. M. Hossain, S. Nirantar, W. Withayachumnankul, T. Ahmed, M. Bhaskaran, S. Sriram, M. Gu, and C. Fumeaux, "Metal-loaded dielectric resonator metasurfaces for radiative cooling," *Adv. Opt. Mater.*, vol. 5, no. 20, p. 1700460, Aug. 2017.

[4] W. C. Chew, *Waves and Fields in Inhomogeneous Media*. Hoboken, NJ, USA: Wiley, 1999.

[5] J.-M. Jin, *The Finite Element Method in Electromagnetics*, 3rd ed. Hoboken, NJ, USA: Wiley, 2014.

[6] Z. G. Qian and W. C. Chew, "A quantitative study on the low frequency breakdown of EFIE," *Microw. Opt. Technol. Lett.*, vol. 50, no. 5, pp. 1159–1162, 2008.

[7] W. Chen, S. Sun, Y. G. Liu, Q. S. Liu, Y. Chen, and J. Hu, "Study of generalized formulation for augmented electric field integral equation with perturbation method," *International Journal of Numerical Modelling: Electronic Networks, Devices and Fields*, p. e2789, 2020.

[8] F. Vico, M. Ferrando, L. Greengard, and Z. Gimbutas, "The decoupled potential integral equation for time-harmonic electromagnetic scattering," *Commun. Pure Appl. Math.*, vol. 69, no. 4, pp. 771–812, 2016.

[9] W. C. Chew, "Vector potential electromagnetics with generalized gauge for inhomogeneous media: Formulation," *Prog. Electromagn. Res.*, vol. 149, pp. 69–84, Sep. 2014.

[10] J. Li, X. Fu, and B. Shanker, "Decoupled potential integral equations for electromagnetic scattering from dielectric objects," *IEEE Trans. Antennas Propag.*, vol. 67, no. 3, pp. 1729–1739, Mar. 2019.

[11] Q. S. Liu, S. Sun, and W. C. Chew, "A potential-based integral equation method for low-frequency electromagnetic problems," *IEEE Trans. Antennas Propag.*, vol. 66, no. 3, pp. 1413–1426, Mar. 2018.

[12] T. E. Roth and W. C. Chew, "Development of stable A-Φ time-domain integral equations for multiscale electromagnetics," *IEEE J. Multiscale Multiphys. Comput. Tech.*, vol. 3, pp. 255–265, Dec. 2018.

[13] A. Poggio and E. Miller, "Integral equation solutions of three-dimensional scattering problems," in *Computer Techniques for Electromagnetics*, ser. International Series of Monographs in Electrical Engineering. Pergamon, 1973, pp. 159 – 264.

[14] Y. Chang and R. Harrington, "A surface formulation for characteristic modes of material bodies," *IEEE Trans. Antennas Propag.*, vol. 25, no. 6, pp. 789–795, Nov. 1977.

[15] T. Wu and L. L. Tsai, "Scattering from arbitrarily-shaped lossy dielectric bodies of revolution," *Radio Sci.*, vol. 12, no. 5, pp. 709–718, Sep. 1977.

[16] S. Sharma and P. Triverio, "Electromagnetic modeling of lossy materials with a potential-based boundary element method," *IEEE Antennas Wireless Propag. Lett.*, 2021 (early access, DOI:10.1109/LAWP.2021.3132626).

[17] T. Xia, H. Gan, M. Wei, W. C. Chew, H. Braunisch, Z. Qian, K. Aygün, and A. Aydiner, "An integral equation modeling of lossy conductors with the enhanced augmented electric field integral equation," *IEEE Trans. Antennas Propag.*, vol. 65, no. 8, pp. 4181–4190, Aug. 2017.

[18] J. D. Jackson, *Classical Electrodynamics*, 3rd ed. Hoboken, NJ, USA: Wiley, 1999.

[19] G. W. Hanson and A. B. Yakovlev, *Operator Theory for Electromagnetics*. New York, NY, USA: Springer-Verlag, 2002.

[20] S. Rao, D. Wilton, and A. Glisson, "Electromagnetic scattering by surfaces of arbitrary shape," *IEEE Trans. Antennas Propag.*, vol. 30, no. 3, pp. 409–418, May 1982.

[21] A. Buffa and S. H. Christiansen, "A dual finite element complex on the barycentric refinement," *Math. Computation*, vol. 76, pp. 1743–1769, 2007.

[22] F. P. Andriulli, K. Cools, H. Bagci, F. Olyslager, A. Buffa, S. Christiansen, and E. Michielssen, "A multiplicative calderon preconditioner for the electric field integral equation," *IEEE Trans. Antennas Propag.*, vol. 56, no. 8, pp. 2398–2412, Aug. 2008.

[23] T. Xia, H. Gan, M. Wei, W. C. Chew, H. Braunisch, Z. Qian, K. Aygün, and A. Aydiner, "An enhanced augmented electric-field integral equation formulation for dielectric objects," *IEEE Trans. Antennas Propag.*, vol. 64, no. 6, pp. 2339–2347, Jun. 2016.

[24] Z. G. Qian, W. C. Chew, and R. Suaya, "Generalized impedance boundary condition for conductor modeling in surface integral equation," *IEEE Trans. Microw. Theory Tech.*, vol. 55, no. 11, pp. 2354–2364, Nov. 2007.

[25] W. C. Gibson, *The Method of Moments in Electromagnetics*. Boca Raton, FL, USA: CRC press, 2014.

[26] J. Song, C.-C. Lu, and W. C. Chew, "Multilevel fast multipole algorithm for electromagnetic scattering by large complex objects," *IEEE Trans. Antennas Propag.*, vol. 45, no. 10, pp. 1488–1493, Oct. 1997.

[27] E. Bleszynski, M. Bleszynski, and T. Jaroszewicz, "AIM: Adaptive integral method for solving large-scale electromagnetic scattering and radiation problems," *Radio Sci.*, vol. 31, no. 5, pp. 1225–1251, Sep. 1996.

[28] Z. Zhu, B. Song, and J. K. White, "Algorithms in FastImp: a fast and wide-band impedance extraction program for complicated 3-D geometries," *IEEE Trans. Comput.-Aided Design Integr. Circuits Syst.*, vol. 24, no. 7, pp. 981–998, Jul. 2005.

[29] D. Güney, T. Koschny, and C. M. Soukoulis, "Reducing ohmic losses in metamaterials by geometric tailoring," *Phys. Rev. B*, vol. 80, p. 125129, Sep. 2009.